Bioprinting 32 (2023) e00285

Contents lists available at ScienceDirect

Bioprinting

journal homepage: www.sciencedirect.com/journal/bioprinting

On the spectrum of transcatheter mitral valve replacement: In silico and in vitro assessment of neo-LVOT area in ViR, ViV and ViMAC

Chiara Catalano [a], Stefano Cannata [b], Valentina Agnese [c], Giovanni Gentile [d], Caterina Gandolfo [b], Salvatore Pasta [a,c,*]

[a] Department of Engineering, Viale delle Scienze, Università degli Studi di Palermo, Palermo, Italy
[b] Department for the Treatment and Study of Cardiothoracic Diseases and Cardiothoracic Transplantation, IRCCS-ISMETT, Palermo, Italy
[c] Department of Research, IRCCS-ISMETT, Palermo, Italy
[d] Radiology Unit, Department of Diagnostic and Therapeutic Services, IRCCS-ISMETT, Palermo, Italy

ARTICLE INFO

Keywords:
Transcatheter mitral valve replacement
Finite element (FE) analysis
Computational fluid dynamics (CFD)
3D printing

ABSTRACT

The assessment of the neo-left ventricular outflow tract (neo-LVOT) area is an essential metric for pre-procedural imaging when screening patients for transcatheter mitral valve replacement (TMVR) eligibility. Indeed, the implantation of transcatheter heart valves for treating failed annuloplasty band ring (ViR), bioprosthesis (ViV) and mitral valve calcification (ViMAC) can lead to a permanent obstruction of the implanted device (namely, LVOT obstruction). In this study, in silico computational modeling and 3D printing were used to quantify the neo-LVOT area and the resulting hemodynamic outcomes of TMVR. We first simulated the deployment of the SAPIEN 3 Ultra device (Edwards Lifesciences, Irvine, CA) and then evaluated the pressure drop near the LVOT obstruction using computational fluid dynamics. The neo-LVOT area was largest in patients with ViR (453.4 ± 58.1 mm^2) compared to patients with ViV (246.6 ± 109.5 mm^2) and ViMAC (155.6 ± 46.1 mm^2). The pressure drop near the LVOT obstruction differed among patients with TMVRs and significantly correlated with the magnitude of the neo-LVOT area (R = −0.761 and P-value = 0.047). The present study highlights the potential of in silico and 3D printed models for planning TMVR procedures and for carrying out a risk evaluation of the device protrusion into the left heart when treating failed mitral valves.

1. Introduction

Transcatheter mitral valve replacement (TMVR) has gained increased interest as a novel and less invasive treatment for patients with significant regurgitation and high risk of conventional mitral valve surgery [1,2]. TMVR is currently carried out using transcatheter heart valves designed for the non-invasive treatment of the aortic valve. A spectrum of TMVR procedures is used in off-label applications in the mitral space, including mitral valve-in-ring (ViR), valve-in-valve (ViV), or valve-in-mitral annulur calcification (ViMAC) [3–6]. However, the structure and function of the mitral valve are complex, being characterized by a highly-dynamic, non-planar and non-circular annulus with the subvalvular apparatus. TMVR consists of delivering a transcatheter heart valve that allows for adequate sealing and anchoring whilst being able to accommodate the failed mitral valve annulus and its motion during the beating of the heart. The procedure carries the unfavorable risk of narrowing the left ventricular outflow tract (LVOT) as the device permanently displaces the native anterior mitral valve leaflet towards the intraventricular septum [7,8]. This protrusion of the device into the original LVOT (LVOT obstruction) represents a potentially fatal complication, with an incidence of approximately 7%–9% in TMVR procedures [9]. Current clinical trials indicate that LVOT obstruction is an exclusion criterion for nearly 50% of patient candidates for TMVR [10].

The risk of LVOT obstruction is different among specific patient populations [11]. In the setting of failed bioprosthesis (i.e. ViV), the risk of LVOT obstruction may vary depending on the original implant, with height rather than size playing an important role in the extension of the obstruction. In this group, the risk of LVOT obstruction is in the range of 2.2%–2.6% in TMVR patient cases [12]. Similarly, mitral ViR is associated with high rates of obstruction, occurring in 5%–8% of procedures in a multicenter study [6]. The type of annuloplasty band ring (i.e. rigid

* Corresponding author. Industrial Bioengineering, Department of Engineering, University of Palermo and 3D printing and Virtual Reality Laboratory, Department of Research, IRCCS Mediterranean Institute for Transplantation and Advanced Specialized Therapies, Via Tricomi, 5, Palermo, Italy.
E-mail addresses: spasta@ismett.edu, salvatore.pasta@unipa.it (S. Pasta).

https://doi.org/10.1016/j.bprint.2023.e00285
Received 21 February 2023; Received in revised form 12 May 2023; Accepted 26 May 2023
Available online 27 May 2023

versus flexible) can influence the level of device adaptation to the failed mitral valve, but ring compliance appears not to change the patient outcome [11]. In patients with ViMAC, LVOT obstruction is the most important factor for adverse events and the mortality rate is reported to be as high as 45% in post-TMVR clinical studies [11].

Pre-procedural computed tomography (CT) imaging is the only tool available for risk stratification of patients with borderline anatomies at high risk of developing LVOT obstructions. Successful predictions of risk rely on the utilization of CT images to measure the minimal area confined by the implanted device and the interventricular septum corresponding to the LVOT obstruction [8]. This region, called the "neo--LVOT", represents a good predictor of TMVR-related complications [12]. While the value of converting the CT dataset into anatomically accurate models for in vitro device bench testing has been demonstrated [13], in silico predictions of neo-LVOT have been poorly investigated [14–17]. Indeed, patient-specific simulations may address the shortcomings of a pure geometric analysis, like the approach proposed by Blanke and collaborators [8] to estimate the neo-LVOT area from pre-TMVR CT imaging.

In this context, this study aims to quantify the neo-LVOT area in TMVRs and compare the biomechanical performance of implanted devices among patients with ViR, ViV and ViMAC. The correlation of neo-LVOT area measurements done by post-TMVR CT imaging with in silico predictions and 3D printed models are assessed. Computational fluid dynamics are also used to quantify the pressure drop near the narrowed LVOT and, thus, the hemodynamic impairment induced by the device obstruction.

2. Methods

2.1. Patient study population

The patient study group is represented by 7 patients who underwent transapical TMVR procedures with the SAPIEN 3 Ultra device (Edwards Lifesciences, Irvine, CA) at the organ-transplant institute ISMETT IRCCS. The full spectrum of TMVR procedures in different types of failed mitral valve were considered, including 2 patients with ViR, 3 patients with ViV, and 2 patients with ViMAC. Patients with ViR had a previous history of annuloplasty with the Sorin Memo 3D ring (Sorin Group Italia SrL, Italy), followed by multiple episodes of mitral valve failure (ViR-Case#1) or left ventricular dysfunction (ViR-Case#2). Patients with ViV presented with mitral valve failure of a previous bioprosthetic heart valve (Carpentier-Edwards Perimount Magna, Edwards Lifesciences, Irvine, CA) and had a high risk of re-do surgery. Severe mitral valve calcification characterized elderly patients with ViMAC. Pre-operative ECG–gated CT imaging was carried out in all patients to assess the mitral valve annulus and, thus, evaluate the optimal size of the intended SAPIEN 3 Ultra. The spatial resolution of the CT imaging was $0.488 \times 0.488 \times 0.625$ mm. In all cases, the SAPIEN 3 Ultra was placed with 1/3 of the height in the left atrial position and the remaining part inside the LVOT, as suggested by the manufacturer guidelines [18]. For 5 patients, post-TMVR CT imaging was performed to measure the neo-LVOT area. For the other patients, a second CT scan in the short follow-up period was not feasible because of renal dysfunction in the context of advanced age. In these cases, the neo-LVOT area was calculated using the Mimics Enlight TMVR structural planning tool (Materialise, BE) and the pre-TMVR CT images. The study was approved by the local ethical committee, and all patients signed informed consent prior to enrollment.

2.2. Segmentation

For all patients, ECG–gated CT images at the end-systolic phase were segmented using the medical imaging software Mimics (v21, Materialise, BE) [19]. Semiautomatic thresholding using several colored masks was used to reconstruct the left heart (i.e. both atrium and ventricle) and the proximal aortic root. Segmentation was initiated by thresholding on the axial view and then fine tuning of the initial colored mask was performed using both coronal and sagittal views. While the left myocardial wall was segmented, solid models of both the left atrium and aorta were obtained, protruding the luminal surface mask by 4 mm and 2 mm, respectively. Segmentation was also developed for the band ring in ViR and the bioprosthesis in ViV cases. For ViMAC, the severe calcification pattern near the mitral valve annulus was distinctly segmented from the left heart mask. Smoothing and refinement were adopted to improve mesh quality whilst preserving the native heart anatomy. For ViR and ViMAC, the mitral valve was modeled using a parametric model and anatomic measurements described previously by our group [20]. Specifically, the length of mitral valve leaflets was measured at CT scan (see Table 1) and then used to model the free edges of the mitral valve in the Grasshopper toolbox of Rhinoceros (v.7.1, McNeel & associates, WA, USA). Thus, two surfaces interpolating the mitral valve boundaries were realized to model both the anterior and posterior mitral valve leaflets. All anatomic parts were then meshed with tetrahedral elements with different refinements (see Table 1A) using the ICEM meshing tool (v2021, Ansys Inc, PA, USA).

2.3. Patient-specific models

For the sake of simplicity, the left atrium and aorta were assumed to be a quasi-incompressible Neo-Hookean material with descriptors of $C10 = 0.17$ MPa and $D1 = 0.3$ MPa^{-1}. Linear elastic material properties were used for calcification, as in other studies ($E = 10$ MPa and $\nu = 0.475$) [21,22]. Both active and passive material properties were used for the myocardial wall, as in a similar study based on a Living Heart Human Model [15,23]. The active stress in the cardiac fiber direction was generated by a time-varying elastance model, which was activated using a fictitious temperature field during the simulation of the cardiac beat. The passive left-ventricular behavior was mimicked using the Ogden and Holzapfel anisotropic hyperelastic constitutive law [24], which has been used in several cardiac simulation studies [25,26]. Myocardial fiber direction was provided using a local coordinate system, while a fiber angle of ±60 deg from the epicardium (positive value) to the endocardium (negative value) was implemented. For the mitral valve, the anisotropic hyperelastic material model proposed by Holzapfel–Gasser–Ogden was adopted with material parameters based on literature data and a fiber orientation of 13 deg [27]. Table 2A summarizes the material descriptors for the myocardium and mitral valve. For the myocardium and left atrium, a mesh resolution of 0.5 mm was adopted to capture the complex geometrical shape of the patient anatomy.

Table 1
Clinical demographic, device size and post-TMVR measurement of neo-LVOT.

	Age (yrs)	Annulus Size (mm)	Mitral Valve Length (mm)	Device Size (mm)	neo-LVOT (mm^2)
ViR-Case#1	70	20.4–25.3	15.7–12.7	26	348.4
ViR-Case#2	71	23.2–25.4	18.0–10.3	23	455.8
ViV-Case#1	84	29.1–31.2	/	29	318.1
ViV-Case#2	74	24.5–25.2	/	26	462.1*
ViV-Case#3	78	21.9–22.7	/	26	147.3
ViMAC-Case#1	71	12.7–24.9	8.7–10.9	23	154.4
ViMAC-Case#1	82	22.7–21.1	7.4–9.2	26	110.2*

Note: for annulus size, the minimum and maximum dimensions are taken; for mitral valve, the posterior and anterior leaflets are reported; *indicates measurements based on pre-TMVR CT images and Mimics Enlight software.

Table 1A
Material parameters adopted for the device and isotropic materials; E = Young modulus; ν = Poisson coefficient; C10 = material constant; D1 = incompressibility factor σ_y = yield stress; σ_{ult} = ultimate tensile stress; ε_p = plastic strain; μ = viscosity; D = density.

	E (MPa)	ν	C10 (MPa)	D1 (MPa^{-1})	σ_y (MPa)	σ_{ult} (MPa)	ε_p	μ (Pa s)	D (kg/m^3)	Element Number (thousand)
Left Atrium		0.49	0.17	0.3					1060	18.5–19.8
Aorta			0.17	0.3						18.4–24.5
Calcification	10	0.47							2000	11.1–19.7
Band Ring									8000	9.5–10.2
Bioprosthesis			1.7	0.65					1060	27.1–28.8
S3 Ultra - Stent Wire	233e+3	0.35			414	930	0.45		8000	59.2
Sealing Skirt	55	0.49			6.6	6.6	0.6		8000	3.5–3.7
Balloon	600	0.3							1060	62.8
Fluid								3.7×10^{-3}	1060	1.2e+3–1.7e+3

2.4. Band ring, bioprosthesis and SAPIEN 3 ultra models

For patients with ViR, the band geometry was obtained by sweep protrusion of a circular curve perpendicular to the band ring centerline derived from ECG–gated CT images. The cross-section of the circular curve had a diameter of 3 mm. The constitutive material descriptors reported by Morganti et al. [28] were used to model the Nitinol material of ViR cases. Tetrahedral elements with a size of 0.8 mm were used to mesh the band ring geometries. Wire connections were developed to link the band ring to the left heart anatomies.

For patients with ViV, the bioprosthesis stent wire was modeled using a curve spline centered on the bioprosthesis mask seen at CT imaging and then modeled using beam elements with a circular cross-section of 1 mm. The cobalt-chromium alloy of the stent wire was modeled using Von Mises plasticity and isotropic hardening using literature data [29]. Apart from the stent wire, the bioprosthesis was assumed to be a fabric polyester material using a Neo-Hookean model (C10 = 1.7 MPa and D1 = 0.65 MPa^{-1}) [30]. The device was then meshed with tetrahedral elements, with the beam elements describing the stent wire tied to the bioprosthesis model.

The SAPIEN 3 Ultra and balloon delivery systems were used to mimic the TMVR described previously by our group [14]. In brief, the metallic frame of the 26 mm SAPIEN 3 Ultra was meshed with nearly 60,000 structured-hexahedral solid elements with reduced integration (C3D8R). The 23 mm and 26 mm devices were obtained as scaled versions of the 26 mm model. As for the bioprosthesis, the cobalt-chromium alloy of the stent frame was assumed to have Von Mises plasticity and isotropic hardening. The sealing skirt was obtained by closing the struct cell geometries with several surfaces modeled at mid-thickness of the device frame at the crimped stage. These surfaces were meshed with triangular shell elements assuming a thickness of 0.1 mm and then connected to the device frame using tie contact conditions. Elastic-plastic material properties were adopted to simulate the polyethylene terephthalate material of the sealing skirt [30]. The balloon delivery system was obtained by reverse engineering of photographic images at a known scale to identify the outer profile of the balloon system. Membrane elements (M3D4) with a thickness of 0.1 mm were used for the balloon, which was assumed to be a linear-elastic material (E = 600 MPa and ν = 0.3).

2.5. Finite element model of TMVR

Simulations of the SAPIEN 3 Ultra deployment followed by the cardiac beat were carried out using Abaqus/Explicit finite element solver (v.2020, Dassault Systèmes, FR). The SAPIEN 3 Ultra was crimped using a rigid dodecahedral surface and gradually moved along the radial direction from the nominal device diameter to the final diameter (e.g. 4.5 mm for the 26 mm device). A simulation step (0.1 s) was added to account for the elastic recoil induced by the elastic-plastic behavior of the device frame. A similar approach was adopted to deflate the balloon delivery system by constraining the distal ends in all directions. Once the skirt was modeled, the system was assembled and then positioned in the failed mitral valve. Both frictionless and "hard" normal behavior contact conditions were used to account for the interaction between the device and the balloon.

For deployment, the fluid-cavity approach was used to simulate a volume-controlled device expansion realistically. The fluid material properties were calibrated to ensure the filling of the balloon with the nominal volume recommended by the manufacturer (e.g. 21 mL for the 26 mm device). As boundary conditions, the distal ends of the left atrium and aorta were fixed in all directions. The deployment was carried out with the mitral valve at the open stage and in steady-state conditions. Tie contacts were defined among the anatomic parts, while the general contact algorithm implemented in Abaqus/Explicit was used to account for the anatomic part interactions. After the deployment step (0.5 s), an additional step was added to allow for the elastic recoil of the device caused by the hyperelastic behavior of soft tissue parts. Then a cardiac beat starting from the diastole (0.5 s) and ending with systole (0.3 s) was developed. A mass scaling approach was implemented to reduce the computational cost whilst maintaining the ratio of kinetic energy to internal energy at magnitudes <10%. A Rayleigh damping factor was used to control the dynamic response of the anatomic models and device delivery systems.

2.6. Computational flow analysis

Deformed geometries of the left heart and deployed devices were exported at the end-systolic phase to generate the fluid domain. These were then meshed with tetrahedral elements with a size of 0.6 mm. Laminar flow conditions and non-Newtonian viscosity described by the Carreau model were assumed [31]. Computational flow analyses were carried out using an implicit algorithm in FLUENT (v21, ANSYS Inc., Canonsburg, PA, USA), with SIMPLE for pressure correction and the 2nd order accuracy upwind scheme. For boundary conditions, a flow velocity profile was set at the left atrium while a pressure outlet profile was imposed at the aortic root [16]. Three cardiac beats were simulated to reduce the effect of transient flow on the resulting hemodynamics, and the last cycle was used for flow analysis.

2.7. 3D printing

The upper portion of the left ventricle of each patient was manufactured by 3D printing with the goal of fitting an ideal device and then quantifying the neo-LVOT area by CT imaging. Only the upper portion of the left ventricle was developed to facilitate the positioning of the intended device. The left atrium and aorta were not included in order to achieve an open geometry and, thereby, allow direct visualization of the device obstruction For ViR and ViMAC cases, the band ring and bioprosthesis were integrated in the left heart anatomy of each patient. Stereolithography (SLA) rapid prototyping technology (Form 3B+, Formlabs, MA, USA) was used to realize the model using a rigid grey-colored resin. A layer thickness of 0.05 mm was used to capture the changes in the curvature of the heart models. An ideal cylindrical surface with dimensions similar to the SAPIEN 3 Ultra was manufactured

Table 2A
Material parameters of mitral valve and left ventricle; C10 = material constant of isotropic response; k_1 and k_2 = material constant of fiber response; k = fiber dispersion parameter; a and b = material constants of isotropic response; a_f and b_f = material constants of stiffness in fiber direction; a_{fs} and b_{fs} = material constants of stiffness in sheet direction.

	C10 (MPa)	k_1 (MPa)	k_2 (MPa)	k	a (MPa)	b	a_f (MPa)	b_f	a_s (MPa)	b_s	a_{fs} (MPa)	b_{fs}	C_{a0} (μmol/L)	D (kg/m^3)	Element Number (thousand)
Mitral Valve	1.2e-4	1.1e-3	8.4e-3	8.0e-2	4.0e-1	12.0	5.0e-1	5.0	2.0e-1	2.0	1.1e-2	2.0	2.66	1060	19.8–22.3
Left Ventricle														1060	171.4–185.6

with an elastic resin (shore hardness of 50A and elongation at failure of 160%) and then manually placed in the stiff 3D printed anatomic parts. A CT scan was then carried out on the 3D printed model to measure the neo-LVOT area.

3. Results

Fig. 1 shows the end-systolic deformed shapes of the left heart with implanted devices for three representative patients with ViR, ViV and ViMAC. The neo-LVOT area was calculated using the approach proposed by Blanke et al. [8]. Once the centerline of the aortic root and native LVOT was created, the anatomic geometry was cut with a cross-sectional plane normal to the centerline near the smallest neo-LVOT area seen between the device frame and the myocardial wall. The view from the aortic root clearly highlighted the obstruction induced by the protrusion of the device frame and the permanently displaced mitral valve. Fig. 2 shows a detailed view of the neo-LVOT area for each patient. The patients with ViR had the largest values of neo-LVOT area (average of 453.4 ± 58.1 mm^2, n = 2) compared to patients with severe mitral valve calcification (155.6 ± 46.1 mm^2, n = 2). Patients with ViV had a neo-LVOT area of 246.6 ± 109.5 mm^2 (n = 3). Fig. 3 shows the changes in neo-LVOT area over a cardiac cycle for three patients with ViR, ViV and ViMAC. While a minimal neo-LVOT area was observed at end-systole, the end-diastole had nearly a 48% increase in the magnitude of the neo-LVOT area.

Fig. 4 displays the end-systolic pressure distribution encompassing the neo-LVOT obstruction for all patients who underwent TMVR. We also calculated the pressure drop between the left ventricle and the neo-LVOT region. Pressure distributions demonstrate that the device elongation and displaced mitral valve lead to a narrowing of outflow regions characterized by pressure drops with differences from patient to patient.

Imaging of actual post-TMVR and 3D printed models are shown for a representative patients with ViR (Figs. 5 and 6). Linear regression and Bland-Altman plots were adopted to establish the degree of concordance and agreement of post-TMVR CT measurements of neo-LVOT with those predicted by both in-silico and 3D printed models (Fig. 7). The correlation coefficient was R = 0.992 between post-TMVR CT and computational measurements (95% confidence interval, CI = 0.990–0.996, P-value<0.001) and R = 0.965 between post-TMVR CT and 3D printed models (95% confidence interval, CI = 0.982–0.988, P-value <0.001). Neo-LVOT measured by post-TMVR CT imaging had a bias of ±37.1 units compared to computational predictions (limits of agreement = 2.9–71.3) and bias of ±30.0 units compared to 3D printed replicas (limits of agreement = −55.0 – 115.2).

A linear regression analysis was performed correlating pressure drop predictions with neo-LVOT area as determined by post-TMVR CT imaging (Fig. 8). A negative relationship was found between the CT-related neo-LVOT area and computational pressure drop estimations, with a Pearson correlation coefficient of R = −0.761 and P-value of 0.047.

4. Discussion

The main finding of this study is a deep understanding of prosthesis delivery in failed mitral valves and the resulting LVOT obstruction individualized for each heart, which was determined by the use of in silico modeling and the generation of 3D printed replicas. Accurate pre-procedural assessment of patient suitability for TMVR still remains of paramount importance in diminishing the occurrence of clinically-relevant LVOT obstructions and ultimately adverse events. This study presents the expansion and validation of in silico and in vitro methods for predicting the impact of neo-LVOT area on the structure and hemodynamics of the left heart in patients with TMVR.

In line with previous findings from both clinical studies and basic science [12,32,33], the neo-LVOT area can be assessed using baseline CT data sets in combination with advanced computer simulations and 3D printing techniques. Ooms et al. [34] emphasize the utilization of

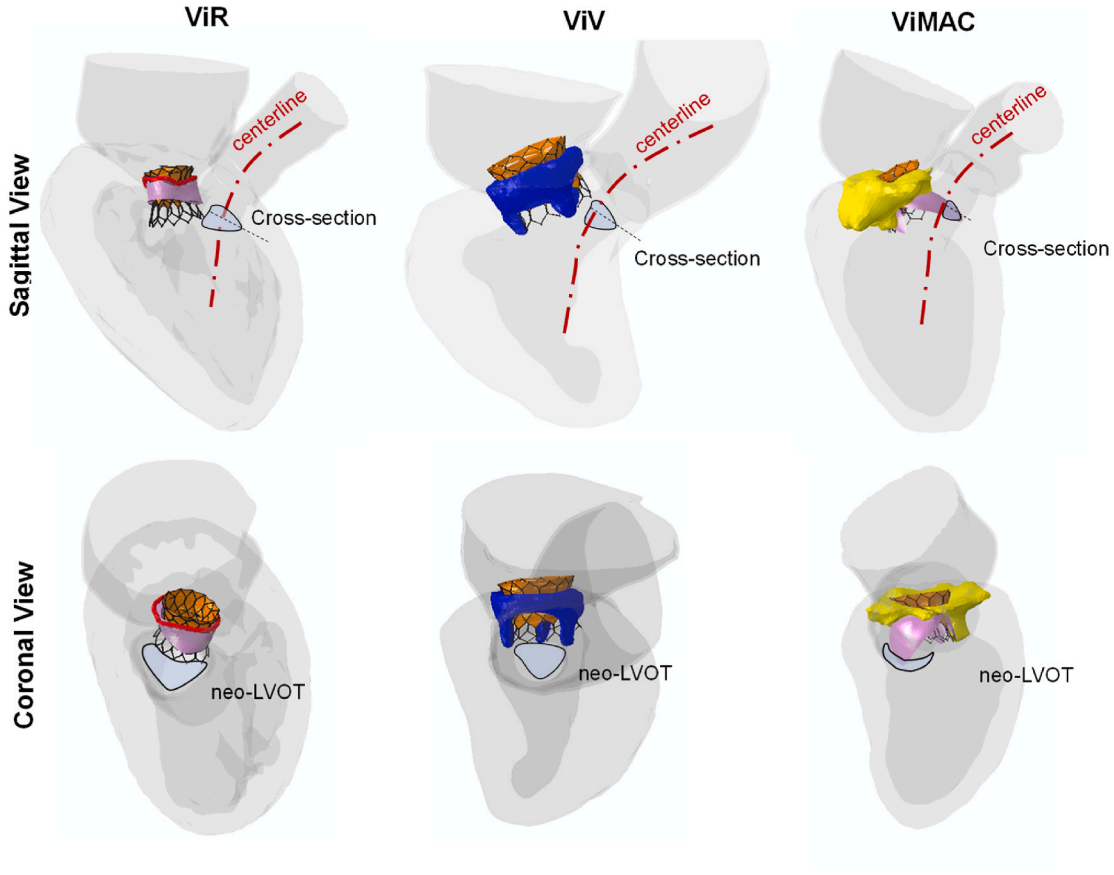

Fig. 1. Different 3D views of LVOT obstruction and its neo-LVOT area for three TMVR patients with ViR, ViV and ViMAC; the centerline and cross-section shows the regions where the neo-LVOT areas are computed.

computational and 3D printed modeling as physicians can benefit from patient-specific risk stratification strategies and hands-on procedural planning. Computational modeling allows estimations of the neo-LVOT area and complements 3D printing, which in turn offers the opportunity to evaluate the device's impact in life-size anatomic replicas. Major findings from in silico report the feasibility of computational fluid dynamics for quantifying the stenotic flow induced by the protruded device into the left ventricular chamber [13,17,35]. Using computational fluid dynamics, an increase in the left ventricular afterloads and the presence of systolic flow disturbances are observed near the neo-LVOT region in models with idealized shapes of LVOT obstruction [36]. Recently, Hill and collaborators [37] have demonstrated in three patients with ViMAC that computational flow analysis can predict the association between the size of the neo-LVOT area and the increase in pressure gradient across the obstruction. The higher the neo-LVOT area is, the lower the pressure drop. They also highlight the potential for thrombus formation near the device implanted in the calcified mitral valve leaflets, as the combination of high shear stress magnitude and long exposure time to shearing may lead to platelet activation and ultimately to early device failure. However, to the best of our knowledge, this is the first study reporting computational findings of TMVRs with degenerated bioprostheses, failed annuloplasty rings and mitral annular calcification. The fact that we have found high values of neo-LVOT areas for patients with ViRs with respect to those in patients with ViV and ViMAC is in agreement with clinical findings [12]. In patients with and without LVOT obstruction, imaging measurements highlight that patients with ViR have significantly higher values of neo-LVOT areas compared to patients with ViMAC [11,12]. Patients with ViV also have lower obstructions than ViR patients. Although there is no established cutoff value that works for all transcatheter heart valves, a neo-LVOT area ranging from 1.7 to 1.9 cm^2 represents a safe condition for delivering the SAPIEN 3 device in a failed mitral valve [11]. In all cases reported here, the neo-LVOT area estimations are above the cutoffs for adverse events associated with LVOT obstructions. We have also found that the pressure drop varies markedly among different types of TMVR procedures. For instance, the patient with ViR and a neo-LVOT area of 412.3 mm^2 had a pressure drop of 7.3 mmHg, which is higher than the patient with ViMAC having an obstruction of 188.2 mm^2 and a pressure drop of 5.6 mmHg. This suggests that factors other than the neo-LVOT area alone may play an important role in the hemodynamic disturbances induced by the implanted device. An interplay between the implanted device and the surrounding myocardial tissue is expected to occur after TMVR. Recent data suggests that the annulus-to-septal distance, the dimension and mass of the left ventricle at end diastole, and myocardial thickness are predisposing factors to a high risk of LVOT obstruction [11]. If such factors are corroborated in a large patient cohort, there will be clear evidence that patient-specific methodologies for the screening of the anatomic suitability for TMVR are needed to quantify the multifactorial risk of LVOT obstruction.

Using CT imaging, two pre-procedural methods for the estimation of the minimum neo-LVOT area have been proposed [35]. In the first method, the neo-LVOT area was assessed by embedding a virtual valve in the CT images, and then the minimum value of the area confined by the virtual valve and the tissue wall was computed by planimetry on the cross-sectional image plane perpendicular to the aortic centerline. Using this method, the cutoff for adverse events related to LVOT obstruction was an area $\leq$170.0 mm^2 [12]. The second method relied on CAD modeling, where a virtual device surface was implanted in the

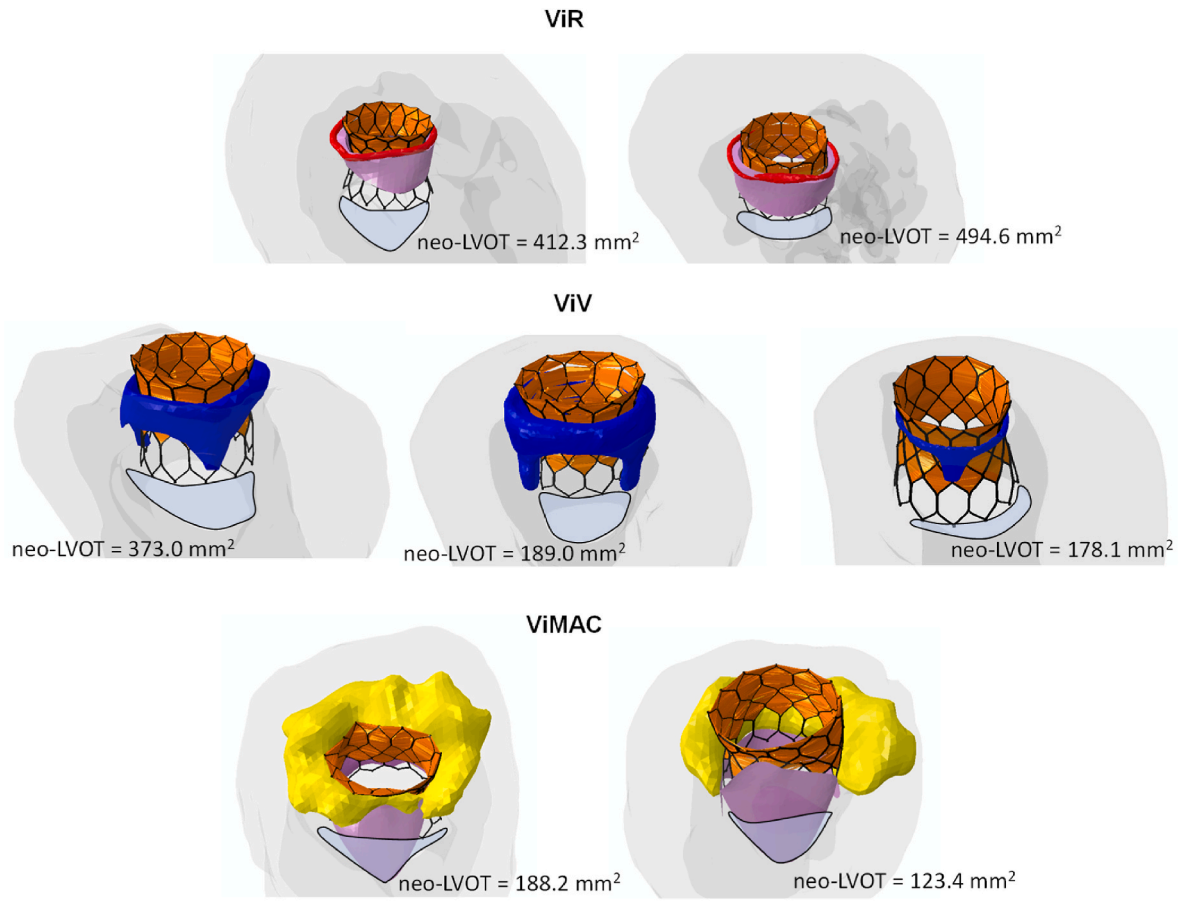

Fig. 2. Specific views from the aortic root showing the neo-LVOT area for each TMVR patients.

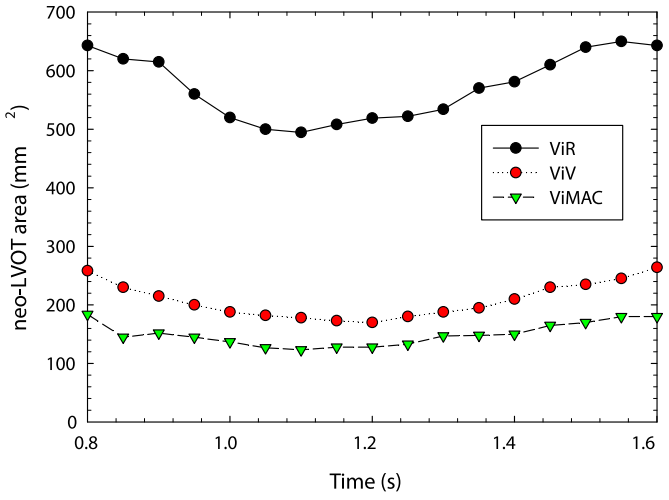

Fig. 3. Profiles of neo-LVOT area changes over the cardiac beat for three representative patients with ViR, ViV and ViMAC; patient with ViR had cardiac beat of 72 bpm, patient with ViV had 65 bpm and patient with ViMAC had 74 bpm.

CT-derived model of the left heart anatomy and was then virtually tested on the screen for assessment of the device obstruction. The CT-derived model was also 3D printed to facilitate the visual inspection of device protrusion into the left heart, thereby overcoming the limitations of 2D imaging and allowing the investigation of different depths and angles of the device deployment. One study using this method revealed a cutoff value of the neo-LVOT area of 189.4 mm^2 as an indicator for complications [34]. While direct comparisons of the clinical accuracy of neo-LVOT predictions in pre- and post-TMVR imaging have demonstrated an excellent correlation with high reproducibility and accuracy [34], the performance of neo-LVOT predictions with CAD virtual manipulation and 3D printing needs to be assessed. In this study, we tested the level of agreement of neo-LVOT area CT-related predictions with both 3D printed models and numerical simulations. Although our findings need to be validated in a large patient cohort, the direct comparison between 3D printed models and CT images allows us to better understand the impact of candidate materials (i.e. rigid versus flexible) for rapid prototyping on the development of accurate replicas. While the calcified plaques, the annuloplasty and the ring can be considered rigid, the heart anatomy is a soft and compliant tissue that ought to be manufactured with flexible materials. It should be noted, however, that the deformed shape of an LVOT obstruction is the result of a balance between the radial forces exerted by the device frame and the elastic recoil of the myocardial tissue.

5. Limitations

This study is limited by the small group of patients undergoing TMVR; indeed, the findings need to be validated in a large patient cohort. TMVR is considered a potential treatment only for elderly patients at risk of conventional mitral valve surgery. A multicenter clinical study is, therefore, recommended to increase the sample size and, hence, the specific patient populations for ViR, ViV and ViMAC. Moreover, post-TMVR CT imaging was not feasible for two of our patients, so the neo-LVOT areas were computed using the pre-TMVR CT and a virtual device model. This may have influenced the comparisons of neo-LVOT areas across different methodologies. Segmentation of patient-specific anatomies included morphological operations and smoothing, which

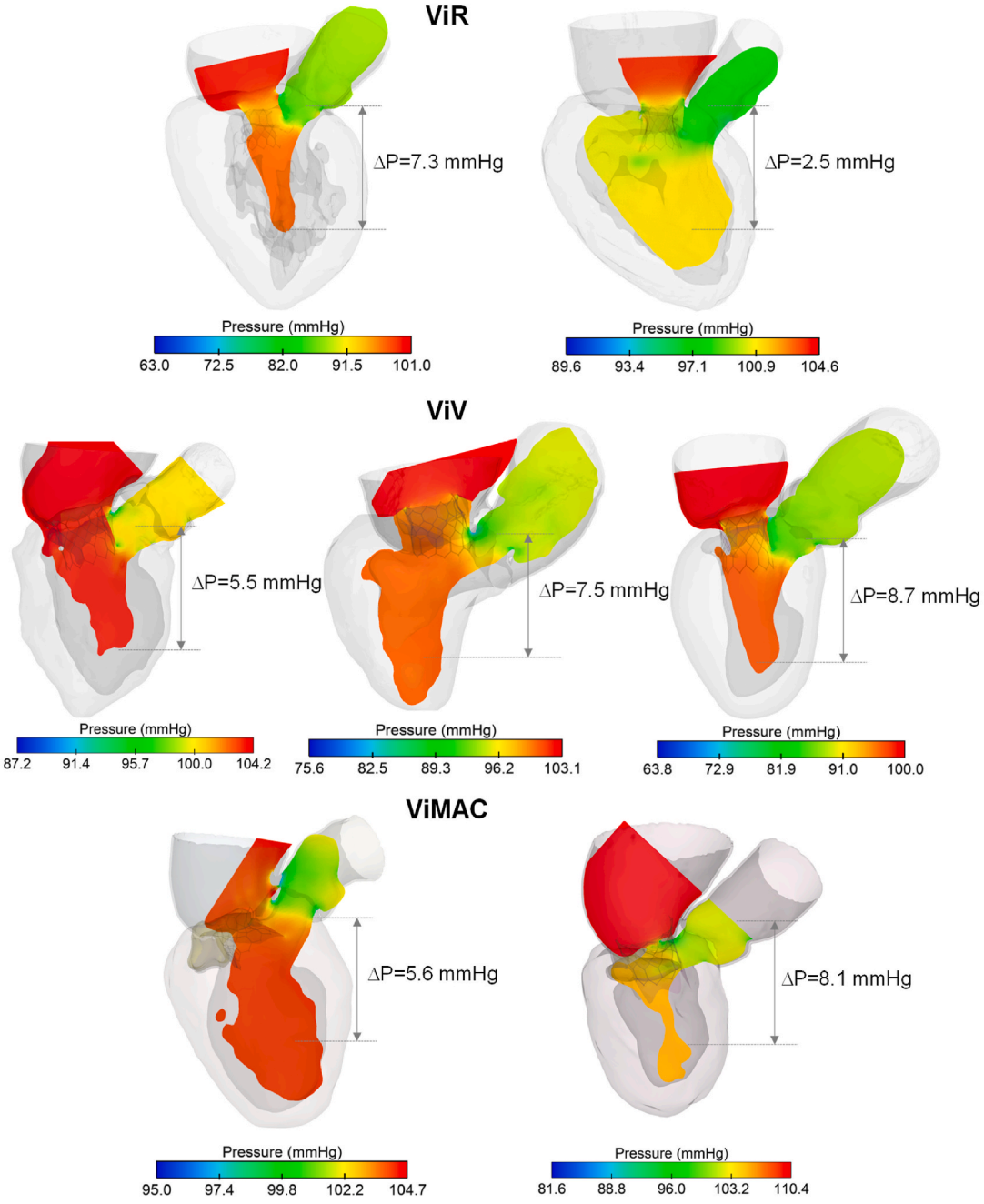

Fig. 4. Map of end-systolic blood pressure showing the impact of LVOT obstruction: the pressure drop was calculated between the left ventricle and neo-LVOT region.

may have altered the final model accuracy. From a computational point of view, the biomechanical response of the left heart during cardiac beating was not calibrated against clinical data. In cardiac simulations, the material properties of both passive and active responses can be iteratively adjusted so that the simulation output can match the end-diastolic and end-systolic left ventricular volume seen by echocardiography [26]. Computational modeling can be utilized to investigate the impact of implantation depth on the risk of LVOT obstruction. However, it should be noted that the manufacturer recommends an optimal implantation depth of one-third the device length on the left ventricle to prevent device migration and potential complications. Finally, 3D printed models were fabricated using a rigid material which did not consider heart compliance nor the deformation occurring when the device is implanted manually. 3D printed model accuracy can be influenced by process parameters such as the light curing, spot diameter compensation and scanning speed and distance. Though the present study represents a step towards the understanding of TMVR, further studies on large patient cohorts and more comprehensive computational models are needed to corroborate our findings. Using a large patient cohort, patient subgroups can be arranged to generate more homogenous patient population and thus reducing the potential bias among TMVR types likely occurring in this study. Future studies should also include a flexible material behavior for developing 3D printed models.

Fig. 5. 3D printed models and related CT imaging of the left heart for the patient with ViR.

6. Conclusion

Using computational modeling and 3D printing, the LVOT obstruction resulting from TMVR was quantified and compared among patients with ViR, ViV and ViMAC. The spectrum of TMVRs in failed bioprosthesis, band ring and mitral valve calcified leaflets can lead to differences in the structural and hemodynamic indicators of an LVOT obstruction. This study further demonstrates the need for patient-specific simulations for pre-TMVR planning and for the assessment of risk induced by the device obstruction in the left heart.

Ethics approval and consent to participate

This study was approved by the IRCCS ISMETT Ethics Committee (approval no. IRRB04/04). All participants provided written informed consent prior to enrolment in the study.

Consent for publication

All authors were fully involved in the study and preparation of the manuscript which contribution originality can be confirmed by members of ISMETT and the University of Palermo. All authors approve the submission.

Availability of data and material

The datasets generated during and/or analysed during the current study are not publicly available due to ethical issues but are available from the corresponding author on reasonable request.

Funding

This study was funded by the grant "Sim4SAPIEN" from Edwards Lifesciences SA (THV-I20-532). Ms Catalano thanks the SimInSitu project (No 101017523) for supporting her research fellowship.

Statements and declarations

Funding: This study was funded by the grant "Sim4SAPIEN" from Edwards Lifesciences SA (THV-I20-532).

CRediT authorship contribution statement

Chiara Catalano: performed the experiment and simulation, wrote

Fig. 6. (A) 3D printed models and related CT imaging of the left heart for the patient with ViR; (B) post-TMVR CT images for the same patient.

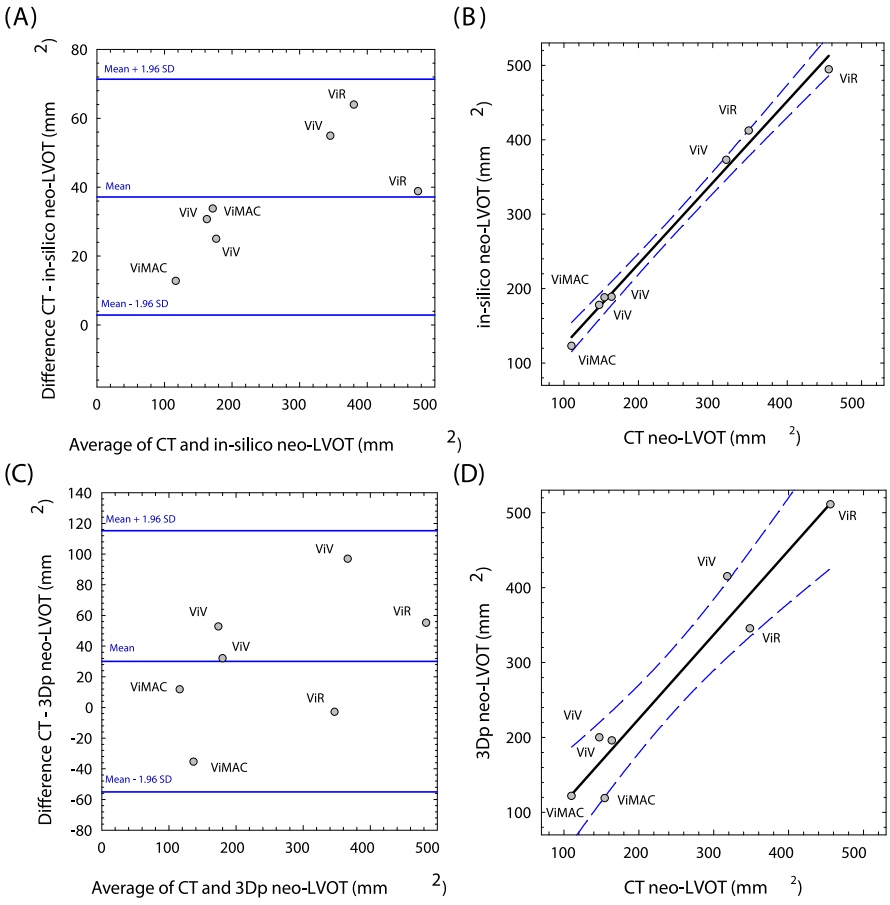

Fig. 7. Regression lines and Bland-Altman comparison between in-silico and post-TMVR CT images (A and B) and between 3D printed (3Dp) models and post-TMVR CT images (C and D).

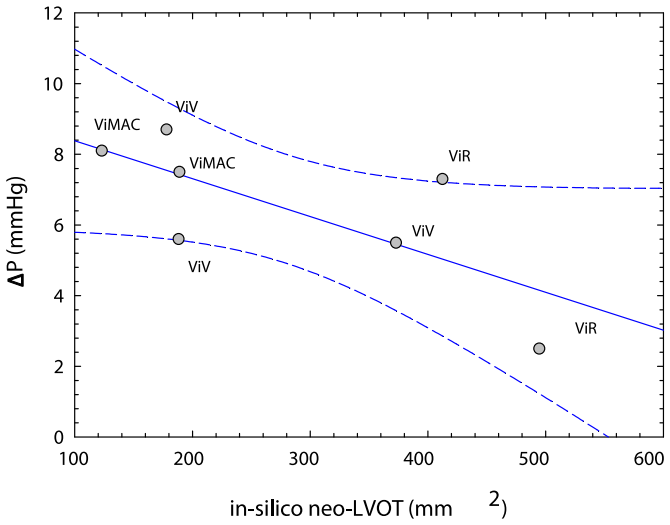

Fig. 8. Linear regression with 95% confidence intervals between the pressure drop and neo-LVOT area resulting from simulations.

the main manuscript text. All authors reviewed the manuscript. **Stefano Cannata:** analyszed data, wrote the main manuscript text. All authors reviewed the manuscript. **Valentina Agnese:** analyszed data, wrote the main manuscript text. All authors reviewed the manuscript, and. **Giovanni Gentile:** collected and analyszed imaging data. **Caterina Gandolfo:** wrote the main manuscript text. All authors reviewed the manuscript, and. **Salvatore Pasta:** wrote the main manuscript text. All authors reviewed the manuscript.

Declaration of competing interest

The authors declare that they have no known competing financial interests or personal relationships that could have appeared to influence the work reported in this paper.

Data availability

The authors do not have permission to share data.

References

[1] V.C. Babaliaros, A.B. Greenbaum, J.M. Khan, T. Rogers, D.D. Wang, M.H. Eng, et al., Intentional percutaneous laceration of the anterior mitral leaflet to prevent outflow obstruction during transcatheter mitral valve replacement: first-in-human experience, JACC Cardiovasc. Interv. 10 (8) (2017) 798–809, https://doi.org/10.1016/j.jcin.2017.01.035.

[2] D.W.M. Muller, R.S. Farivar, P. Jansz, R. Bae, D. Walters, A. Clarke, et al., Transcatheter mitral valve replacement for patients with symptomatic mitral regurgitation: a global feasibility trial, J. Am. Coll. Cardiol. 69 (4) (2017) 381–391, https://doi.org/10.1016/j.jacc.2016.10.068.

[3] M. Guerrero, D. Dvir, D. Himbert, M. Urena, M. Eleid, D.D. Wang, et al., Transcatheter mitral valve replacement in native mitral valve disease with severe mitral annular calcification: results from the first multicenter global registry, JACC Cardiovasc. Interv. 9 (13) (2016) 1361–1371, https://doi.org/10.1016/j.jcin.2016.04.022.

[4] J.M. Paradis, M. Del Trigo, R. Puri, J. Rodes-Cabau, Transcatheter valve-in-valve and valve-in-ring for treating aortic and mitral surgical prosthetic dysfunction, J. Am. Coll. Cardiol. 66 (18) (2015) 2019–2037, https://doi.org/10.1016/j.jacc.2015.09.015.

[5] S.H. Yoon, B.K. Whisenant, S. Bleiziffer, V. Delgado, N. Schofer, L. Eschenbach, et al., Transcatheter mitral valve replacement for degenerated bioprosthetic valves

and failed annuloplasty rings, J. Am. Coll. Cardiol. 70 (9) (2017) 1121–1131, https://doi.org/10.1016/j.jacc.2017.07.714.
[6] S.H. Yoon, S. Bleiziffer, O. De Backer, V. Delgado, T. Arai, J. Ziegelmueller, et al., Outcomes in transcatheter aortic valve replacement for bicuspid versus tricuspid aortic valve stenosis, J. Am. Coll. Cardiol. 69 (21) (2017) 2579–2589, https://doi.org/10.1016/j.jacc.2017.03.017.
[7] S. Alsidawi, M.F. Eleid, C.S. Rihal, V.T. Nkomo, S. Pislaru, Significant LVOT obstruction after mitral valve in ring procedure, European heart journal cardiovascular Imaging 16 (12) (2015) 1389, https://doi.org/10.1093/ehjci/jev235.
[8] P. Blanke, C. Naoum, D. Dvir, V. Bapat, K. Ong, D. Muller, et al., Predicting LVOT obstruction in transcatheter mitral valve implantation: concept of the neo-LVOT, JACC Cardiovascular imaging 10 (4) (2017) 482–485, https://doi.org/10.1016/j.jcmg.2016.01.005.
[9] M.F. Eleid, A.K. Cabalka, M.R. Williams, B.K. Whisenant, O.O. Alli, N. Fam, et al., Percutaneous transvenous transseptal transcatheter valve implantation in failed bioprosthetic mitral valves, ring annuloplasty, and severe mitral annular calcification, JACC Cardiovasc. Interv. 9 (11) (2016) 1161–1174, https://doi.org/10.1016/j.jcin.2016.02.041.
[10] V. Bapat, V. Rajagopal, C. Meduri, R.S. Farivar, A. Walton, S.J. Duffy, et al., Early experience with new transcatheter mitral valve replacement, J. Am. Coll. Cardiol. 71 (1) (2018) 12–21, https://doi.org/10.1016/j.jacc.2017.10.061.
[11] A. Reid, S. Ben Zekry, M. Turaga, S. Tarazi, J.J. Bax, D.D. Wang, et al., Neo-LVOT and transcatheter mitral valve replacement: expert recommendations, JACC Cardiovascular imaging 14 (4) (2021) 854–866, https://doi.org/10.1016/j.jcmg.2020.09.027.
[12] S.H. Yoon, S. Bleiziffer, A. Latib, L. Eschenbach, M. Ancona, F. Vincent, et al., Predictors of left ventricular outflow tract obstruction after transcatheter mitral valve replacement, JACC Cardiovasc. Interv. 12 (2) (2019) 182–193, https://doi.org/10.1016/j.jcin.2018.12.001.
[13] K. Kohli, Z.A. Wei, A.P. Yoganathan, J.N. Oshinski, J. Leipsic, P. Blanke, Transcatheter mitral valve planning and the neo-LVOT: utilization of virtual simulation models and 3D printing, Curr. Treat. Options Cardiovasc. Med. 20 (12) (2018) 99, https://doi.org/10.1007/s11936-018-0694-z.
[14] S. Pasta, S. Cannata, G. Gentile, M. Di Giuseppe, F. Cosentino, F. Pasta, et al., Simulation study of transcatheter heart valve implantation in patients with stenotic bicuspid aortic valve, Med. Biol. Eng. Comput. (2020), https://doi.org/10.1007/s11517-020-02138-4.
[15] S. Pasta, C. Catalano, S. Cannata, J.M. Guccione, C. Gandolfo, Numerical simulation of transcatheter mitral valve replacement: the dynamic implication of LVOT obstruction in the valve-in-ring case, J. Biomech. (2022) 144, https://doi.org/10.1016/j.jbiomech.2022.111337. ARTN 111337.
[16] S. Pasta, S. Cannata, G. Gentile, V. Agnese, M. Pilato, C. Gandolfo, Simulation of left ventricular outflow tract (LVOT) obstruction in transcatheter mitral valve-in-ring replacement, Med. Eng. Phys. 82 (2020) 40–48, https://doi.org/10.1016/j.medengphy.2020.05.018.
[17] P. de Jaegere, R. Rajani, B. Prendergast, N.M. Van Mieghem, Patient-specific computer modeling for the planning of transcatheter mitral valve replacement, J. Am. Coll. Cardiol. 72 (8) (2018) 956–958, https://doi.org/10.1016/j.jacc.2018.05.064.
[18] E. Lifesciences, Edwards SAPIEN 3 Transcatheter Heart Valve with the Edwards Commander System 23/26/29 Mm Sizes - Procedural Training Manual, 2015.
[19] S. Pasta, C. Gandolfo, Pre-operative modeling of transcatheter mitral valve replacement in a surgical heart valve bioprosthesis, Prosthesis 2 (1) (2020) 39–45, https://doi.org/10.3390/prosthesis2010004.
[20] S. Pasta, G. Gentile, G.M. Raffa, F. Scardulla, D. Bellavia, A. Luca, et al., Three-dimensional parametric modeling of bicuspid aortopathy and comparison with computational flow predictions, Artif. Organs 41 (9) (2017) E92–E102, https://doi.org/10.1111/aor.12866.
[21] S. Pasta, S. Cannata, G. Gentile, V. Agnese, G.M. Raffa, M. Pilato, et al., Transcatheter heart valve implantation in bicuspid patients with self-expanding device, Bioengineering 8 (7) (2021) 91.
[22] M. Di Giuseppe, G. Alotta, V. Agnese, D. Bellavia, G.M. Raffa, V. Vetri, et al., Identification of circumferential regional heterogeneity of ascending thoracic aneurysmal aorta by biaxial mechanical testing, J. Mol. Cell. Cardiol. 130 (2019) 205–215, https://doi.org/10.1016/j.yjmcc.2019.04.010.
[23] S. Cutugno, V. Agnese, G. Gentile, G.M. Raffa, A.D. Wisneski, J.M. Guccione, et al., Patient-specific analysis of ascending thoracic aortic aneurysm with the living heart human model, Bioengineering-Basel. 8 (11) (2021), https://doi.org/10.3390/bioengineering8110175. ARTN 175.
[24] G.A. Holzapfel, R.W. Ogden, Constitutive modelling of passive myocardium: a structurally based framework for material characterization, Philos Trans A Math Phys Eng Sci 367 (1902) (2009) 3445–3475, https://doi.org/10.1098/rsta.2009.0091.
[25] J.C. Walker, M.B. Ratcliffe, P. Zhang, A.W. Wallace, B. Fata, E.W. Hsu, et al., MRI-based finite-element analysis of left ventricular aneurysm, Am. J. Physiol. Heart Circ. Physiol. 289 (2) (2005) H692–H700, https://doi.org/10.1152/ajpheart.01226.2004.
[26] J.M. Guccione, L.K. Waldman, A.D. McCulloch, Mechanics of active contraction in cardiac muscle: Part II–Cylindrical models of the systolic left ventricle, J. Biomech. Eng. 115 (1) (1993) 82–90, https://doi.org/10.1115/1.2895474.
[27] W. Sun, W. Mao, B.E. Griffith, Computer modeling and simulation of heart valve function and intervention, Principles of Heart Valve Engineering (2019) 177–211. Elsevier.
[28] S. Morganti, N. Brambilla, A.S. Petronio, A. Reali, F. Bedogni, F. Auricchio, Prediction of patient-specific post-operative outcomes of TAVI procedure: the impact of the positioning strategy on valve performance, J. Biomech. 49 (12) (2016) 2513–2519, https://doi.org/10.1016/j.jbiomech.2015.10.048.
[29] W. Mao, A. Caballero, R. McKay, C. Primiano, W. Sun, Fully-coupled fluid-structure interaction simulation of the aortic and mitral valves in a realistic 3D left ventricle model, PLoS One 12 (9) (2017), e0184729, https://doi.org/10.1371/journal.pone.0184729.
[30] S. Morganti, M. Conti, M. Aiello, A. Valentini, A. Mazzola, A. Reali, et al., Simulation of transcatheter aortic valve implantation through patient-specific finite element analysis: two clinical cases, J. Biomech. 47 (11) (2014) 2547–2555, https://doi.org/10.1016/j.jbiomech.2014.06.007.
[31] G. D'Ancona, A. Amaducci, A. Rinaudo, S. Pasta, F. Follis, M. Pilato, et al., Haemodynamic predictors of a penetrating atherosclerotic ulcer rupture using fluid-structure interaction analysis, Interact. Cardiovasc. Thorac. Surg. 17 (3) (2013) 576–578, https://doi.org/10.1093/icvts/ivt245.
[32] D.D. Wang, M.H. Eng, A.B. Greenbaum, E. Myers, M. Forbes, P. Karabon, et al., Validating a prediction modeling tool for left ventricular outflow tract (LVOT) obstruction after transcatheter mitral valve replacement (TMVR), Cathet. Cardiovasc. Interv. 92 (2) (2018) 379–387, https://doi.org/10.1002/ccd.27447.
[33] D.D. Wang, M. Eng, A. Greenbaum, E. Myers, M. Forbes, M. Pantelic, et al., Predicting LVOT obstruction after TMVR, JACC Cardiovascular imaging 9 (11) (2016) 1349–1352, https://doi.org/10.1016/j.jcmg.2016.01.017.
[34] J.F. Ooms, D.D. Wang, R. Rajani, S. Redwood, S.H. Little, M.L. Chuang, et al., Computed tomography-derived 3D modeling to guide sizing and planning of transcatheter mitral valve interventions, Jacc-Cardiovasc Imag. 14 (8) (2021) 1644–1658, https://doi.org/10.1016/j.jcmg.2020.12.034.
[35] K. Kohli, Z.A. Wei, V. Sadri, A.W. Siefert, P. Blanke, E. Perdoncin, et al., Assessing the hemodynamic impact of anterior leaflet laceration in transcatheter mitral valve replacement: an in silico study, Frontiers in cardiovascular medicine 9 (2022), 869259, https://doi.org/10.3389/fcvm.2022.869259.
[36] A. De Vecchi, D. Marlevi, D.A. Nordsletten, I. Ntalas, J. Leipsic, V. Bapat, et al., Left ventricular outflow obstruction predicts increase in systolic pressure gradients and blood residence time after transcatheter mitral valve replacement, Sci. Rep. 8 (1) (2018), 15540, https://doi.org/10.1038/s41598-018-33836-7.
[37] S.J. Hill, A. Young, B. Prendergast, S. Redwood, R. Rajani, A. De Vecchi, Patient-specific fluid simulation of transcatheter mitral valve replacement in mitral annulus calcification, Frontiers in cardiovascular medicine 9 (2022), 934305, https://doi.org/10.3389/fcvm.2022.934305.